

GEOCHEMISTRY

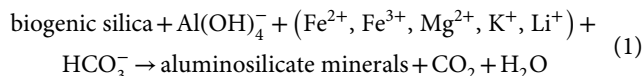
Rapid transformation of biogenic silica to authigenic clay: Mechanisms and geochemical constraints

Simin Zhao^{1†}, Emily M. Saad^{1†}, Rebecca A. Pickering², Pan Liu¹, Hongyan Zuo³, Linduo Zhao⁴, Ellery Ingall¹, Martial Taillefert¹, Christopher T. Reinhard¹, Hailiang Dong⁵, Jeffrey W. Krause^{2,6*}, Yuanzhi Tang^{1*}

Authigenic clay formation during early diagenesis of marine sediments, termed “reverse weathering,” is an important process for regulating ocean pH, seawater chemistry, and atmospheric CO₂ over geologic time scales. Although the importance of reverse weathering has been increasingly recognized, the rates and mechanisms remain poorly constrained. This study investigated the mechanisms, kinetics, and mineral products derived from diatom biogenic silica. We show the formation of Fe(II)-bearing smectite and mica in 40 days, the most rapid process and first specific mineral phases reported to date. Unraveling the kinetics and mechanisms of authigenic clay formation suggests that reverse weathering is far more dynamic and responsive to changes in ocean chemistry than previously envisioned, with a potential to impact marine alkalinity cycling on a shorter timescale.

INTRODUCTION

Reverse weathering in marine environments, proposed in the 1960s (1–4), was suggested to be a major component of the missing burial sinks of silicon (Si) and alkalinity (HCO₃[−]) produced during terrestrial weathering. It follows the general reaction of



Through the reaction, amorphous biogenic silica [e.g., diatom silica originating from the upper water column or surface-lit sediments; hereafter (bSi)] transforms into authigenic aluminosilicates (5), consuming cations (e.g., Fe, Mg, K, and Li) and alkalinity (HCO₃[−]) while producing CO₂. CO₂ production during reverse weathering has been suggested to affect ocean pH and global climate over geological time and is incorporated into biogeochemical models tracing climate evolution in Earth’s history (3, 6–10). In addition, cation consumption by marine authigenic clay formation is considered as an important modulator for seawater chemistry (11, 12). The impact of these processes is only beginning to be considered in global elemental budgets and Earth system biogeochemical models (8–10, 13–15). For instance, the marine Si budget has been long observed to be out of balance with burial fluxes insufficient to match inputs (16). Recent studies estimated that the Si burial flux due to marine reverse weathering is 4.5 to 4.9 Tmol Si/year (15, 17), which potentially balances the marine Si deficit. These recent estimates make reverse weathering the second largest sink among all currently recognized output processes within the global marine Si budget (15). Upward revision of the magnitude of marine reverse weathering in the global Si budgets may have

important implications for the associated carbon cycle (e.g., seawater alkalinity), coastal acidification, sequestration of other elements (e.g., Fe, Al, Mg, and K), and direct and indirect feedbacks on marine primary productivity, global climate (15, 16, 18), and anthropogenic interventions of the carbon cycle with geoengineered climate solutions (19, 20).

The understanding of reverse weathering in marine systems has improved in the past several decades, with seminal studies demonstrating the effectiveness of reverse weathering for transforming bSi and the possibility of rapid clay mineral formation, in contrast to previous frameworks in which reverse weathering was neglected or thought to occur on the order of 10³–10⁶ years (21). These studies relied on indirect evidence from field observations to indicate rapid Si and Al reactions, e.g., stoichiometric relationships between dissolved Al and Si in sediment pore waters (22–24). Strong associations of bSi with authigenic clay minerals and cation-rich aluminosilicate coatings on diatom frustules in deep-sea and deltaic sediments implied the importance of diatoms in this process (21, 25, 26), with subsequent Si stable isotope measurements providing evidence for the connection between sediment bSi with authigenic clay mineral formation (27). The direct evidence of reverse weathering has also been obtained through experimental incubation of bSi with sediments (5, 28, 29), which shows bSi alteration and formation of authigenic K- and Fe-rich mica- or smectite-like clays within 10 to 36 months (5, 28, 29).

However, despite these advances, substantial uncertainty remains around the controlling geochemical factors, kinetics, mechanisms, and specific reaction products of reverse weathering. First, the function of potential reactant species and the phases of reaction products are poorly constrained. Despite the commonly observed association between Fe and aluminosilicate phases (29), the roles of Fe- and Al-containing species in the transformation process remain elusive. The authigenic clay phases produced from reverse weathering are small particles (e.g., submicron sized) (29–31), making their characterization and detection highly challenging using traditional techniques (32, 33). The characterization of authigenic clays in field samples is further confounded due to the mixing with abundant detrital clays (34). The identification of these authigenic products has previously relied on laboratory incubations, usually based on

¹School of Earth and Atmospheric Sciences, Georgia Institute of Technology, Atlanta, GA 30332-0340, USA. ²Stokes School Marine and Environmental Sciences, University of South Alabama, Mobile, AL 36688, USA. ³Department of Geology & Environmental Earth Science, Miami University, Oxford, OH 45056, USA. ⁴Illinois Sustainable Technology Center, University of Illinois Urbana-Champaign, Champaign, IL 61820, USA. ⁵China University of Geosciences, Beijing, Beijing 100190, China. ⁶Dauphin Island Sea Lab, Dauphin Island, AL 36528, USA.

*Corresponding author. Email: yuanzhi.tang@eas.gatech.edu (Y.T.); jkrause@disl.edu (J.W.K.)

†These authors contributed equally to this work.

compositions from extraction methods and scanning electron microscopy with energy dispersive spectroscopy (SEM-EDX) (26, 35), and the comprehensive mineral identifications were challenging or lacking (26). Second, previous laboratory incubations, which ranged in duration from 10 to 36 months (5, 26, 29) only examined the reaction products at the end point. Thus, the time-course dynamics are almost entirely unknown. Third, specific reaction mechanisms are poorly constrained. Although authigenic clay diagenesis is thought to involve dissolution and reprecipitation reactions, with the participation of Al, Si, and cations (e.g., Mg and Fe; Eq. 1) (28, 29), the roles of specific elements and their speciation (e.g., oxidation state, dissolved versus solid phase) remain unclear.

To improve the mechanistic understanding of the reverse weathering processes, controlled laboratory experiments were conducted using diatom bSi under representative marine dissolved Fe(II) concentrations and combinations of Fe- and Al-hydroxide minerals (hereafter Fe/Al hydroxides) in artificial seawater. Experiments were conducted in anoxic conditions using custom-built two-chamber reactors, which separate bSi from Fe/Al hydroxides by a dialysis membrane (fig. S1). This reactor design allows for the mixing solely of dissolved species (e.g., Si, Fe, and Al) and separates the transformed bSi from the Fe/Al hydroxide phases to facilitate systematic characterization. All experiments were initially amended with 150 μM dissolved silicic acid [$\text{Si}(\text{OH})_4$, denoted as dSi] to mimic field-observed pore water $\text{Si}(\text{OH})_4$ concentration (27, 28, 35). Experimental groups with and without bSi substrate were included. Both groups were incubated with dissolved Fe(II) concentrations of 0, 100, or 1000 μM , with or without Fe and/or Al hydroxides (denoted as Fe, Al, or FeAl). Group I (with bSi) was used to constrain the dissolution and reprecipitation processes and phase change of bSi. Group II (without bSi) was used to interpret the $\text{Si}(\text{OH})_4$ precipitation mechanism observed in Group I. Table 1 and table S1 summarize treatment conditions and sample labels. Duplicate treatments were run for all 24 combinations. Details on experimental preparation and setups are in Materials and Methods. With this experimental matrix, we directly elucidated the reaction mechanisms and the roles of Fe and Al and their associated minerals in authigenic clay

formation, constrained the reaction rates, and revealed the specific authigenic minerals formed.

RESULTS

Rapid authigenic clay formation after 1 month of incubation

SEM analyses after 40 days of incubation showed notable transformation of bSi in the presence of 1000 μM Fe(II) (Fig. 1B), as compared to no obvious morphological transformation in the absence of Fe(II) (Fig. 1A). Energy dispersive x-ray spectroscopy (EDX) analyses (Fig. 1B) showed Fe, Si, and O distributions overlapping with bSi, suggesting Fe precipitation on and/or incorporation into bSi frustules, consistent with earlier observations (29, 36). In the presence of both 1000 μM Fe(II) and Al hydroxide, bSi was extensively altered and showed distinct morphological changes during alteration (Fig. 1C). The overlapping of Fe and Al EDX maps (Fig. 1C) indicated Fe and Al precipitation on and/or incorporation into bSi (29, 36). In addition, aggregated curvy flaky precipitates in rosette morphology rich in Fe, Si, Al, and Mg with small amounts of Ca were observed on bSi for 1000Fe(II) + bSi + Al (Fig. 1D) and 1000Fe(II) + bSi + FeAl treatments (Fig. 1E), suggesting the formation of authigenic clay phases. The authigenic phases showed average Fe/Si ratio at 0.27 and 0.56 (table S2), repetitively, for 1000Fe(II) + bSi + Al and 1000Fe(II) + bSi + FeAl treatments, in line with the expected range for Fe-bearing phyllosilicate minerals (37). EDX maps of individual authigenic phases without the visual presence of nearby/underlying bSi residue (i.e., near complete transformation of bSi) also showed an overlapping composition of Si with Fe and Al (fig. S2). For bSi treated with 100 μM Fe(II) and minerals, SEM analysis showed a lower alteration extent for bSi, and no obvious layered phases could be discerned.

Experimental groups in the 1000 μM Fe(II) treatments showing signs of secondary mineral formation under SEM were further analyzed by synchrotron x-ray diffraction (XRD) and high-resolution transmission electron microscopy (HRTEM) for identification. Harvested solids from the bSi chamber of the 1000Fe(II) + bSi + Al treatment showed the appearance of an additional broad diffraction

Table 1. Summary of treatment conditions and sample labels with bSi for group I. All treatments contain 150 μM background dissolved silica, $\text{Si}(\text{OH})_4$. “+” stands for the addition of the reactant. Note that group II is identical as group I, except for the absence of bSi.

Treatment group	Dissolved $\text{Si}(\text{OH})_4$ (μM)	Dissolved Fe(II) (μM)	bSi	Fe(OH) ₃	Al(OH) ₃	Sample label
Group I (with bSi)	150	0	+			0Fe(II) + bSi
	150	0	+	+		0Fe(II) + bSi + Fe
	150	0	+		+	0Fe(II) + bSi + Al
	150	0	+	+	+	0Fe(II) + bSi + FeAl
	150	100	+			100Fe(II) + bSi
	150	100	+	+		100Fe(II) + bSi + Fe
	150	100	+		+	100Fe(II) + bSi + Al
	150	100	+	+	+	100Fe(II) + bSi + FeAl
	150	1000	+			1000Fe(II) + bSi
	150	1000	+	+		1000Fe(II) + bSi + Fe
	150	1000	+		+	1000Fe(II) + bSi + Al
	150	1000	+	+	+	1000Fe(II) + bSi + FeAl

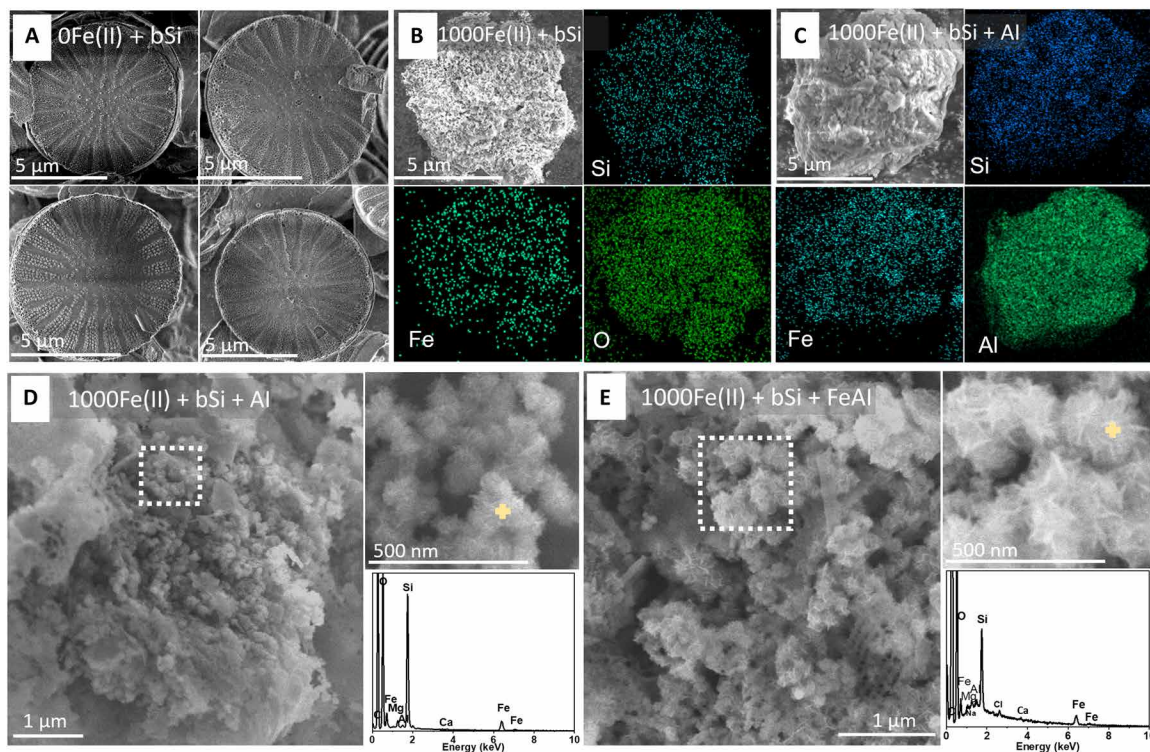


Fig. 1. Representative SEM images and EDX elemental maps of reacted bSi after 40 days. (A) 0Fe(II) + bSi, (B) 1000Fe(II) + bSi, (C) 1000Fe(II) + bSi + Al, and the morphology and EDX spectra of neoformed phases in 1000Fe(II) + bSi + Al (D) and 1000Fe(II) + bSi + FeAl (E) treatments. No changes in morphology were observed in 0 μM Fe(II) treatment (A), whereas bSi were extensively altered and elemental association of Fe, Si, and O were observed in [(B) and (C)]. Flake-shaped rosette clusters of authigenic phases were observed in [(D) and (E)], with both phase rich in Fe, Si, Al, and Mg with small amounts of Ca. Dashed areas in [(D) and (E)] show zoomed view with EDX spectra taken at the cross point.

peak at ~ 7.8 Å (Fig. 2A), suggesting the formation of clay phase(s) with large interlayer spacing. The broadening of this peak is likely due to small particle size and/or overall poor crystallinity of the bulk phase (38), consistent with SEM observation (Fig. 1, D and E) that the authigenic phase is at a size < submicron level. Additional peaks in the d_{060} region were also observed for 1000Fe(II) + bSi + Al and 1000Fe(II) + bSi + FeAl at 1.57 and 1.54 Å, respectively (Fig. 2B), indicating the formation of trioctahedral smectite clays (37, 38). HRTEM analyses were further conducted on the harvested solids from bSi chamber of 1000Fe(II) + bSi + Al treatment and confirmed the formation of smectite phases (Fig. 3A). Specifically, both tabular (Fig. 3A, location 1) and curvy flaky neoformed phases were observed (Fig. 3A, location 2). Clay mineral crystal morphological features are unique characteristics used as criteria to identify individual species in the clay mineral family (39). The observed curvy morphology at location 2 (Fig. 3A) and bulky curvy rosette aggregates growing on the edges of bSi by SEM (Fig. 1E) suggest potential turbostratic structure and expandable layers, which are key characteristics of smectite (39). The composition from EDX showing a Ca-bearing aluminosilicate composition also suggests a typical feature of smectite where Ca resides as interlayer cation (38). Selected area electron diffraction (SAED) analysis at location 2 (Fig. 3A) showing the presence of six d-spacings at 0.45, 0.26, 0.22, 0.17, 0.15, and 0.12 nm confirmed the formation of 2:1 phyllosilicates (40). Collectively, with the bulky trioctahedral smectite feature indicated by XRD, morphological feature by SEM, Ca-bearing aluminosilicate

composition by EDX, and the structure confirmation from TEM and SAED, the major authigenic mineral phase is identified to be Fe(II)-rich smectite. However, EDX spectrum for the phase at location 1 showed the authigenic phase to be mainly composed of Fe, Mg, Al, K, and Si with relatively high K content. SAED analysis showed the presence of similar six d-spacings at 0.45, 0.26, 0.22, 0.17, 0.15, and 0.12 nm. Based on the combined EDX composition (K-rich and Al-rich aluminosilicate phase), SAED pattern, and the tabular morphology suggesting potentially a nonexpandable feature, the phase in location 1 is best identified as Fe(II)-rich muscovite (Fig. 3A). The elemental composition (table S2) showing an pervasive Fe/Si ratio range of 0.19 to 0.41 also suggests a common Fe/Si ratio for Fe-bearing smectite [e.g., Fe/Si < 0.5 (37)], although the 1000Fe(II) + bSi + FeAl treatment exhibited positions with Fe/Si ratio exceeding 0.5, which are more likely Fe-muscovite composition [e.g., Fe/Si ratio up to ~ 1 (41)]. Although Fe-muscovite has been identified at location 1, its presence is considered to be a localized instance, supported by multiple lines of evidence. We postulate Fe-muscovite to be at minor/small amounts as such phases typically form through alteration of smectites during later stages of diagenesis (13, 31, 42), accompanied by exchanging of interlayer cations from, e.g., Ca^{2+} to K^+ . We therefore think that the authigenic products contain a mixture of phases with Fe(II)-rich smectite as the bulk major phase and minor occurrences of Fe(II)-rich muscovite. In addition, porous morphological features of diatom bSi were observed (Fig. 3A), confirming clay growth on bSi. In comparison, the no

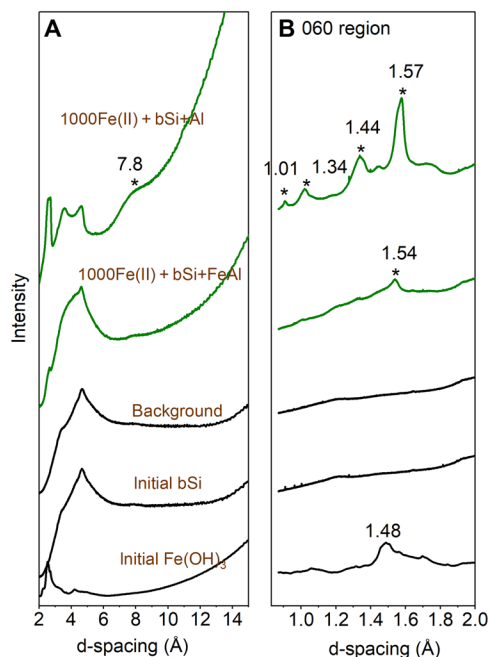


Fig. 2. Synchrotron XRD analysis ($\lambda = 0.39433 \text{ \AA}$) of reacted solids from 1000Fe(II) + bSi + Al and 1000Fe(II) + bSi + FeAl treatments after 40 days. Reacted solids were taken from bSi chamber of the two-chamber reactor compared to initial Fe(OH)₃, bSi, and background from the glass capillary. Asterisks indicate peaks from the neoformed phase. (A) shows a broad d-spacing and (B) shows a zoomed view of the d₆₀₀ region from (A).

mineral control of the 1000 μM Fe(II) treatment [1000Fe(II) + bSi] showed only altered bSi and Fe/Mg/Ca/Si-rich phases without evidence of crystallization (Fig. 3B), consistent with SEM-EDX observation (Fig. 1B).

Authigenic clay formation mechanism revealed by solution evolution

The transformation of bSi to clay observed in this study is further supported by the time evolution of dissolved Si(OH)₄ and Fe(II) (Fig. 4), which demonstrates the complex interactions between the dissolution of solid phases (bSi, Fe hydroxide, and Al hydroxide) and the consumption of dissolved phases [Si(OH)₄, Fe(II), Al] through processes such as sorption and reprecipitation. Thus, we define the observed dissolved Si(OH)₄ concentration, [Si(OH)₄], as the apparent dissolution of bSi, which is the net result of bSi dissolution and consumption.

In the presence of bSi and no Fe(II), [Si(OH)₄] reached 1039 μM in 40 days (bSi; Fig. 4B), consistent with the thermodynamically predicted solubility of amorphous silica under the experimental conditions of this study (43) and observations of asymptotic [Si(OH)₄] in marine sediment porewaters (44, 45). Treatments containing Al hydroxide substantially reduced [Si(OH)₄] at steady state (Fig. 4B). Specifically, the presence of Al hydroxide (bSi + Al) and Fe + Al hydroxides (bSi + FeAl) decreased [Si(OH)₄] by 16 and 28%, respectively. The presence of Fe hydroxide (bSi + Fe) showed less influence, with only 9% decrease in [Si(OH)₄] compared to the no mineral control (bSi) (Fig. 4B).

In the presence of bSi and Fe(II), the concentrations of Fe(II) and Si(OH)₄ at steady state both decreased. For 100 μM Fe(II)

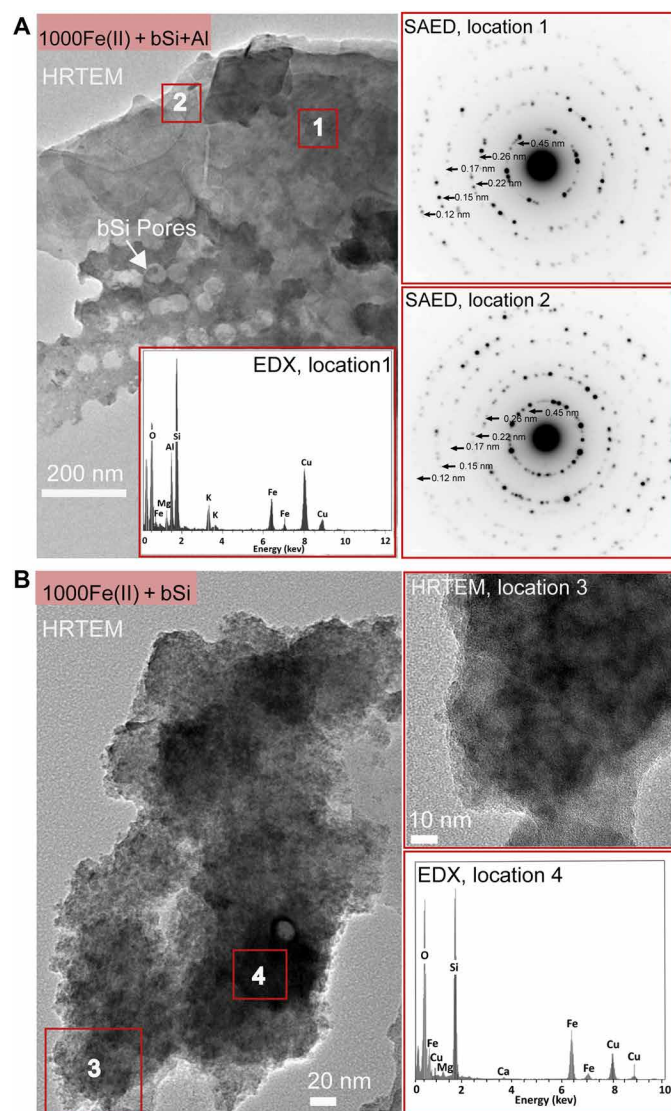


Fig. 3. Representative HRTEM images and corresponding SAED and EDX patterns from 1000Fe(II) + bSi + Al and 1000Fe(II) + bSi treatments after 40 days.

Solids were harvested from the bSi side of the two-chamber reactor. (A) bSi was extensively altered to form authigenic mineral phases. White arrow indicates the porous morphology of residual diatom bSi. SAED patterns of locations 1 and 2 show six d-spacings at 0.45, 0.26, 0.22, 0.17, 0.15, and 0.12 nm, characteristic of 2:1 phyllosilicates. EDX spectrum of location 1 shows a composition consistent with Fe-muscovite dominated by Si, K, Fe, Al, and Mg with high K content. (B) bSi was altered to amorphous cation-bearing phase. A zoomed view of location 3 shows no fringe lattice. EDX spectrum of location 4 shows that the amorphous phase is mainly composed of Si, Fe, Ca, and Mg. Copper signal is from the TEM grid.

treatments, all Fe(II) was removed from solution within ~20 days (Fig. 4C), consistent with the PHREEQC modeling that the system was oversaturated with respect to Fe(II)-silicate phases including e.g., smectite, greenalite, illite, Fe-muscovite (46), and likely involved Fe(II) precipitation. For 1000 μM Fe(II) treatments, all reactions showed substantial but not complete Fe(II) removal (Fig. 4E). The addition of Fe and Al hydroxides showed no systematic effects on Fe(II) removal in the 100 and 1000 μM Fe(II) treatments (figs. S3A and S4, C and E). For 100 μM Fe(II) treatments, the steady

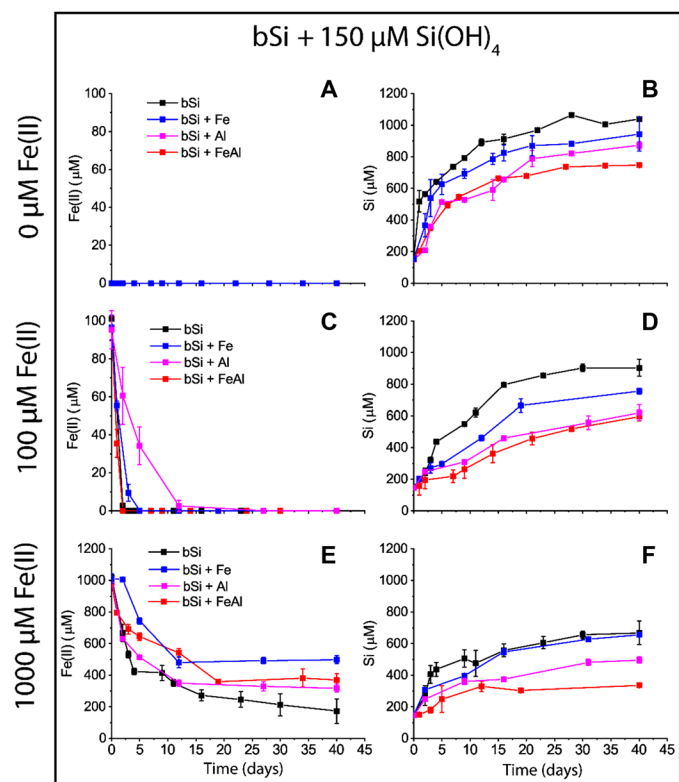


Fig. 4. Time evolution of dissolved Fe(II) and apparent dissolved Si in the presence of bSi and 150 μM initial dissolved $\text{Si}(\text{OH})_4$. Top (A and B), middle (C and D), and bottom panels (E and F) are treatments with 0 μM , 100 μM Fe(II), or 1000 μM Fe(II). The prefixes of 0Fe(II), 100Fe(II), and 1000Fe(II) in sample labels are omitted for the top, middle, and bottom panels for succinctness. Error bars represent SD of duplicate treatment.

state $[\text{Si}(\text{OH})_4]$ in the no mineral control (bSi) decreased to $904 \pm 54 \mu\text{M}$ (Fig. 4D). The presence of minerals further decreased steady-state $[\text{Si}(\text{OH})_4]$ value, i.e., bSi + Al at $620 \pm 50 \mu\text{M}$, bSi + FeAl at $596 \pm 27 \mu\text{M}$, and bSi + Fe at $756 \pm 19 \mu\text{M}$ (Fig. 4D). A similar inhibition effect by dissolved Fe(II) was observed in 1000 μM Fe(II) treatments, with all the 1000 μM Fe(II) treatments (Fig. 4F) showing lower $[\text{Si}(\text{OH})_4]$ than their corresponding samples of no Fe(II) (Fig. 4B) and 100 μM Fe(II) treatments (Fig. 1D). Specifically, steady state $[\text{Si}(\text{OH})_4]$ for the no-mineral control (bSi) decreased by 36% to $668 \pm 75 \mu\text{M}$ in the presence of 1000 μM Fe(II) (Fig. 1F) compared to the no Fe(II) treatment (Fig. 4B). The Al hydroxide treatment (bSi + Al) further decreased $[\text{Si}(\text{OH})_4]$, whereas Fe hydroxide treatment (bSi + Fe) showed less of an effect on $[\text{Si}(\text{OH})_4]$ (Fig. 4F). Relative to the corresponding no Fe(II) groups, steady-state $[\text{Si}(\text{OH})_4]$ in the 1000 μM Fe(II) groups decreased by 43, 54, and 31% for the Al hydroxide (bSi + Al), Fe + Al hydroxides (bSi + FeAl), and Fe hydroxide (bSi + Fe) treatments, respectively. The initial rate of apparent silica dissolution was calculated by fitting a linear regression to the $[\text{Si}(\text{OH})_4]$ profile during the first ~ 7 days. Compared to the bSi-only control, the initial rates of apparent silica dissolution were reduced by the presence of Fe(II) and Al/Fe hydroxides (fig. S3B).

In the 150 μM $\text{Si}(\text{OH})_4$ treatments with no added bSi (experimental treatments dSi), the presence of Al hydroxide and dissolved

Fe(II) accelerated $\text{Si}(\text{OH})_4$ consumption (fig. S4, B, D, and F) likely due to adsorption and precipitation. In the absence of Fe(II) or Fe/Al hydroxides, $[\text{Si}(\text{OH})_4]$ in the dSi treatment persisted at 150 μM throughout the experiment but was reduced in the presence of Al hydroxide (+Al) and Fe + Al hydroxide (+FeAl) treatments, respectively (fig. S4B). In the presence of Fe(II), $[\text{Si}(\text{OH})_4]$ was further consumed (fig. S4, D and F). In the 100 μM (fig. S4D) and 1000 μM Fe(II) dSi treatments (fig. S4F), $[\text{Si}(\text{OH})_4]$ was reduced to 94 ± 5 and $96 \pm 0 \mu\text{M}$ at steady state, respectively, and the addition of Fe + Al hydroxides (+FeAl), Fe hydroxide (+Fe), or Al hydroxide (+Al) further reduced $[\text{Si}(\text{OH})_4]$. The consumption of $[\text{Si}(\text{OH})_4]$ was accompanied by a decrease of Fe(II) (fig. S4, C and E) and dissolved Al (discussed below), suggesting the precipitation of Si in the dSi treatments by Fe(II) and Al.

Dissolved Al concentrations in 0 μM Fe(II) treatments, with and without bSi, showed no consistent trends over time except for occasional spikes (fig. S5A), likely due to the concurrent dissolution and reprecipitation. The 100 and 1000 μM Fe(II) treatment groups, with or without the presence of bSi, also showed occasional spikes of dissolved Al (fig. S5, B and C) but at smaller amplitude than the 0 μM Fe(II) treatment. In addition, in the control experiment containing only 100 μM Fe(II), 30 μM dissolved Al, and 150 μM $\text{Si}(\text{OH})_4$ (“dissolved only”), Al was completely removed from solution within 1 day (fig. S4B), consistent with thermodynamically predicted oversaturation with respect to Fe(II)-silicates, Al-silicates, and amorphous Al-minerals under these conditions (46).

DISCUSSION

With the observed formation of Fe-bearing smectite and muscovite after the 40-day incubation in the presence of Fe(II), Al hydroxide, bSi, and dissolved $[\text{Si}(\text{OH})_4]$, below, we further interpret the formation mechanism from both the source and sink perspectives (Fig. 5), reveal the authigenic clay products and formation timescale, and discuss the implications for the coupled carbon-silicon cycle.

Authigenic clay formation mechanism

Sources: Fe and Al sources

We tested Fe and Al phases as key reactants in reverse weathering, which has been suggested by multiple field studies (28, 29, 36) but for which direct evidence and mechanistic understanding have been lacking. The Fe sources (Fe(II) and Fe(III)-mineral) used in this study are representative of Fe(II) produced in marine sediments by biotic/abiotic reductive dissolution of Fe oxyhydroxides and Fe(III)-bearing Fe oxyhydroxides $[\text{Fe}(\text{OH})_3]$ (28, 29, 36, 47). In marine sediments, the source of Al mainly comes from the dissolution of Al flocs and Al minerals [such as Al oxyhydroxide, clay minerals, and feldspars (48, 49)]. Dissolved Al concentrations in marine sediments are typically very low, i.e., nanomolar level (e.g., 100 to 300 nM) (22). However, as local, if the transient production of higher dissolved Al (via the aforementioned dissolution pathways) (approximately micromolar level) could occur (50, 51), then it would lead to the rapid precipitation of secondary minerals as observed in this study. There are many potential mineral phases that could supply dissolved Al and Fe to sediment pore waters. For this study, common Fe- and Al-containing hydroxide phases were chosen to illustrate the process and the potential influence of these phases on reverse weathering.

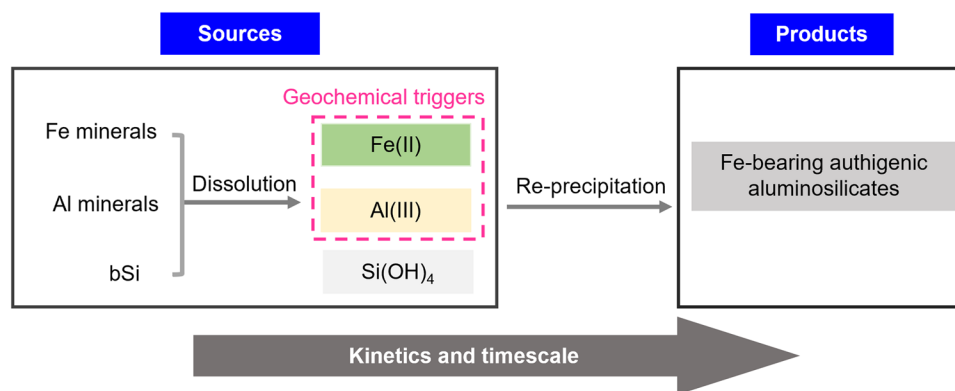


Fig. 5. Conceptual illustration of the mechanisms involved in the formation of authigenic clay revealed by this study. The mechanism involves the sources [dissolved Fe(II), Al(III), and Si(OH)₄] from dissolution of solid phases and products formed via reprecipitation.

bSi dissolution

Reverse weathering reactions during early diagenesis require a Si source. The efficiency of bSi recycling can be a constraint, e.g., lower efficiency in colder temperatures (52, 53). While sediment bSi can include microplankton [e.g., diatoms and Rhizaria (26)] and siliceous sponge spicules (54), diatoms dominate modern bSi production (15, 55, 56). In this study, we observed a decrease in apparent bSi dissolution (quantified as asymptotic [Si(OH)₄]) in the presence of dissolved Fe(II) and Fe/Al-containing minerals, consistent with the inferences from previous studies (discussed below). The influence of Al on bSi dissolution was evident in the Al hydroxide treatments regardless of Fe(II) concentration, which resulted in lower initial rates of apparent silica dissolution (fig. S3B) and final dissolution extent (Fig. 4). A similar effect was observed with Fe(II), where the magnitude of the effect increased with increasing Fe(II) concentration from 100 to 1000 μM. However, Fe hydroxide treatments showed less suppression of apparent bSi dissolution. The decreased [Si(OH)₄] in the presence of dissolved Fe(II), Al hydroxide, or Fe + Al hydroxides [~300 to 700 μM Si(OH)₄ equilibrium concentration] (Fig. 4, B, D, and F) are close to pore water [Si(OH)₄] reported for deltaic and oceanic sediments (36). In addition, in the absence of bSi, Al hydroxide and Fe(II) exerted the strongest control over [Si(OH)₄] precipitation (fig. S4, B, D, and F).

The decrease in steady-state [Si(OH)₄] mimics the inverse relationship between pore water [Si(OH)₄] and the ratio of lithogenic minerals to bSi in marine sediments (57), where lithogenic phases affect the Si(OH)₄ thermodynamic equilibrium (36). Such a [Si(OH)₄] decrease in sediments has been previously suggested to result from absorption (58) or incorporation of dissolved ions into bSi resulting in reduced bSi dissolution (29) and precipitation by dissolved Al (22). Over the 40-day experiment, our results showed that when Fe(II) was 1000 μM, the observed bSi alteration product was enriched in Fe (Figs. 1 and 3) and slightly enriched in Mg and Ca (Fig. 3). This cation incorporation processes likely contributed to the observed decrease in bSi dissolution compared to the no Fe(II) treatment. Compared to Fe(II), the Fe hydroxide treatment did not suppress bSi dissolution to the same degree (Fig. 4, B, D, and F). This may reflect that Fe(III) incorporation in bSi is less favorable (59), consistent with the idea that dissolved Fe(II), as opposed to Fe(III), can suppress the dissolution rate of bSi (59). Al incorporation into bSi has also been shown to reduce its solubility (60, 61), as prior work showed lower bSi dissolution extent

with higher diatom frustule Al/Si ratios (52). Based on the observed Al association with the altered bSi phase in the Al hydroxide treatment (Figs. 1 and 4), our results further demonstrate rapid Al-induced inhibition of bSi dissolution. The bSi surface is negatively charged (58), which should readily absorb dissolved cations, such as Fe(II) and Al(III). The strong structural association of Fe and Al with bSi (Figs. 2 and 4) further supports the inhibition of bSi dissolution due to the incorporation of these elements.

The dissolution of bSi, and subsequent build-up of [Si(OH)₄] in marine sediments, is further governed by the interplay between Si release and removal mechanisms. Authigenic mineral formation has been proposed to explain the decreases in porewater [Si(OH)₄] relative to saturation (2, 36, 57, 58). Our study showed that in the absence of bSi, [Si(OH)₄] notably decreased in the presence of Al hydroxide and/or dissolved Fe(II) (fig. S4, B, D, and F). At the studied pH of 7.5, the removal of Si(OH)₄ by the Al hydroxide can result from adsorption of Si(OH)₄ to the positively charged Al(OH)₃ (62) and/or coprecipitation of dissolved Al and Si(OH)₄. The presence of Fe(II) could have triggered the coprecipitation of Fe(II) and Si(OH)₄, explaining the overall lower extent of bSi dissolution as compared to no Fe(II) treatments. In the presence of bSi, Si sequestration by authigenic mineral formation was observed. The Fe(II) and Al hydroxide treatments (bSi + Al) were among those with the lowest [Si(OH)₄] [496 ± 20 μM for 1000 μM Fe(II) treatment; Fig. 4F], and the neoformed precipitates were identified as Si-rich clay (Fig. 3). Overall, our results provide clear evidence of rapid Si(OH)₄ sequestration by authigenic mineral formation, which is likely a dominant mechanism for decreased [Si(OH)₄] in marine sediment pore waters (63, 64).

Sinks: The reprecipitation of Si(OH)₄ to form authigenic clay minerals

Although authigenic clay mineral formation has been commonly recognized to involve dissolution and reprecipitation processes with the participation of Al, Si, and cations (e.g., Mg, Ca, and Fe) (28, 29), direct evidence for such a clay mineral formation mechanism is lacking. Our results showed that the dissolution of bSi and input of dissolved Fe(II) and Al was followed by the reprecipitation of Si(OH)₄ to form an authigenic clay on bSi. As discussed above, dissolved Fe(II), Al, and Si(OH)₄ are sources for authigenic clay formation. SEM and TEM observations (Figs. 1 and 3) of the authigenic phase formed in bSi-containing experimental chamber showed porous bSi frustule fragments and the associated neoformed clay

phase, supporting the precipitation of clay on bSi. This precipitation outcome is consistent with a previously proposed diagenetic pathway involving frustule alteration and conversion to authigenic clay (26, 35). The precipitation of dissolved Si, Al, and Fe(II) is also supported by the precipitation in the dSi experiment (fig. S3, A to F) triggered by Fe(II) and Al.

Despite the previously acknowledged importance of Fe in reverse weathering (5, 28, 29), the role of Fe concentration and speciation [i.e., Fe(II) versus Fe(III)] has remained elusive. Michalopoulos and Aller (28) directly observed the transformation of sand and FeOOH-coated sand to a Fe-K-rich phase. Subsequent studies also found authigenic phases from altered bSi to be Fe-rich [Michalopoulos *et al.* (5)]. Soluble Fe(II) has been suggested to be more favorable for early diagenesis due to its higher mobility (36). Michalopoulos and Aller (28) assumed that Fe in the Fe-K-rich mica-like mineral was primarily Fe(II) as the dissolved Fe(II) concentration was high in the anoxic Amazon shelf sediment they used for the experiment. The formation of another Fe-bearing clay mineral—greenalite resulted from incubation of high Fe(II) and dissolved Si concentrations without Al, simulating Precambrian seawater condition—also indicated the important roles of Fe(II) in diagenesis (65). Loucaides *et al.* (29) observed Fe association with diatom frustules incubated with field sediments, but not in their laboratory-incubated diatom frustules. These authors attributed this discrepancy to oxic laboratory conditions (29), which resulted in the formation of Fe(III) oxyhydroxides, while the more reducing natural conditions resulted in Fe(II) incorporation into diatom frustule. Here, we show the formation of the authigenic clay mineral phase even without the presence of the Fe(III)-mineral Fe(OH)₃ (Fig. 2). This suggests that Fe(III) minerals do not play a notable role in rapid authigenic clay mineral formation. Instead, the presence of soluble Fe(II) exerted an important role in inducing Si precipitation (Fig. 1 and fig. S3). Thus, we infer that under our experimental conditions, Fe(II), rather than Fe(III)-minerals, was a major direct control on rapid authigenic clay formation. In sedimentary environments, however, Fe(II) is expected to be rapidly produced via microbial Fe cycling where Fe(III)-bearing minerals and organic matter are sufficient (47, 66).

Previous laboratory incubations and field studies found a strong association of Al with bSi as authigenic precipitates (29). The role of Al in inducing precipitation is supported by our results, as the 1000Fe(II) + bSi + Al treatment showed crystalline authigenic clay formation, while the 1000Fe(II) + bSi treatment showed no authigenic clay formation in the same time frame. The precipitation of Si(OH)₄ by Al is also supported in the incubation of dSi (fig. S3, B, D, and F), in which the presence of Al hydroxide resulted in the highest consumption of Si(OH)₄, likely via adsorption and coprecipitation. The experimental apparatus ensured that the neoformed Fe-Al-Si (smectite and muscovite) phase (Figs. 2 and 3) in the bSi-containing chamber could only result from the diffusion of dissolved Al through the membrane from the Al hydroxide-containing chamber (fig. S1). The dissolved Al dynamics observed (fig. S4) suggest that the dissolution and reprecipitation reactions were rapid and not resolved by our sample interval of 2 to 7 days.

Our results highlight the roles of Fe(II) and Al in triggering Si(OH)₄ precipitation and authigenic clay formation. They also provide direct evidence for previously proposed mechanisms and recent field observations of the coupled Fe and Al cycles with Si and authigenic clay formation in deltaic environments (28, 36, 67). Although we identified the participation of other cations (Mg, K, and

Ca) in the authigenic clay formation, these cations did not appear to play rapid driving roles under our experimental conditions (artificial seawater at pH 7.5) as the general presence of these cations in artificial seawater in all control groups without Fe(II) treatment did not induce rapid authigenic clay formation. The finding is consistent with the understanding of cation site participation in clay formation. Specifically, Mg²⁺ could substitute octahedral sites with Fe²⁺/Al³⁺, and Al³⁺ could substitute Si⁴⁺ in the tetrahedral sites, accompanied with K⁺ and Ca²⁺ uptake as interlayer charging-balancing ions during the formation of Fe-bearing clay (13). The finding of Al-Si rich euhedral crystalline phases containing small amounts of Na⁺ and Mg²⁺ resulted from a 10-month incubation of bSi with terrestrial sediments likely imply similar roles of cation participation (29). However, in natural marine settings with diverse geochemistry conditions and fluctuations in local cation concentrations, pH, salinity, and precursor clays, these cations could play more important driving roles in authigenic clay formation. For example, the observed Mg-smectite and talc formation in saline environments with pH higher than 8.2 (68) or sedimentary conditions with a pH ~8.7 (69) suggest whether Mg²⁺ can exert driving roles of authigenic clay formation might highly depend on pH and salinity (68–71). In addition, the evolution of glauconite is highly associated with K⁺ uptake into the Fe-smectite clay precursor, highlighting an important role of K⁺ (13). Therefore, how pre-existing clay and the inclusion of other cations might alter the kinetics and product type need further elucidation.

Products and timescale of authigenic clay formation

Through controlled laboratory incubations and physical isolation of bSi from other mineral reactants (fig. S1), we were able to characterize initial clay mineral products of reverse weathering. Robust identification of clay type is difficult as common Fe-rich clays have similar structures and chemical compositions. For example, Fe-smectites, Fe-bearing illite, and Fe-muscovite have similar structures and only slight variations in chemical composition. They can also transform into each other during diagenesis (e.g., smectite to illite and mica) and/or form mixed-layer phases (38, 72, 73). Glauconite is a common sedimentary clay that consists such mix layered Fe-smectite and Fe-mica via alteration of smectite precursors, commonly found in continental shelf and deep marine environments (31, 74). By combining the morphological characteristics, XRD diffraction patterns, and SAED diffraction patterns with EDX-derived chemical compositions, we identified the experimentally derived clay product to be mainly Fe(II)-bearing smectite with small amounts of Fe(II)-bearing muscovite, both of which are Fe(II)-rich phyllosilicate phases (Fig. 4). The finding is consistent with the proposed mica-type mineral products in field incubations of FeOOH-coated quartz by Michalopoulos and Aller (28) and Fe-smectite-like phases reported in field observations (26, 31). To our knowledge, this is the first direct identification of specific authigenic clay phases formed during early diagenetic reverse weathering reactions.

The timescale of authigenic clay formation (<40 days) observed here was considerably shorter than previously observed timescales (10 to 36 months) (5, 28, 29). This is consistent with the inferred reverse weathering reaction rates at timescale within weeks and months from porewater compositions and Si-Al stoichiometric relations (22, 24, 75) and porewater isotopic signatures combined with reaction-transport modeling (50). However, our findings provide direct evidence with observed crystalline authigenic clay products

that help address the uncertainty of resulting phases (e.g., the observed porewater stoichiometric relationship could also arise from crude amorphous precipitation). Although the abiotic experiment here applied organic coating-removed diatoms to mimic coating removal in natural conditions, this removal is not expected to cause divergent rate from natural settings for the following two reasons. First, organic coating removal by natural heterotrophic bacteria can occur quickly (e.g., <2 weeks), and bacteria-mediated Si generation is similar though not as rapid as that of organic coating-removed frustules by acid cleaning (76). Second, the optimized low-temperature plasma-ashing coating-removing approach applied in this study can sustain both SiO₂ structure and high specific surface area (77), such that the dissolution rate of plasma-ashed bSi is close to that of raw bSi. The dissolution rate of plasma-ashed bSi is one magnitude lower than that derived from conventional harsh cleaning methods (e.g., nitric acid, hydrochloric acid, peroxide, and/or baking). Note that the short timescales of ~40 days for the reverse weathering process in this study is substantially longer than the ion exchange time of <40 hours (fig. S6) across the dialysis membrane of the experimental reactor (fig. S1). Time-course data reported here provide insights on the factors affecting the rate of early diagenesis. As discussed above, both dissolution and reprecipitation exert roles in the diagenetic timeline. bSi dissolution affects the Si source for precipitation and the concentration stabilized after 30 to 40 days (Fig. 4). Previous studies have shown that the bSi dissolution rate is mainly affected by the surface area and charge of different diatom species (58). Although our study only used one diatom species as a representative bSi source, its surface area (~50 m²/g) is typical of diverse diatom species (78), but a factor of 3 to 6 lower than other biosiliceous structures, which may be allochthonous in marine coastal systems [e.g., phytoliths, (79)]. As for the controlling factor in Al hydroxide dissolution, Al(OH)₃ dissolution was estimated to be shorter than our sampling interval (2 to 7 days) (fig. S4). In terms of precipitation, the effects of mineral substrates (e.g., bSi or extra mineral phases in natural sediments) and presence of microbes may also facilitate the diagenetic process. Together, these results provide a basis to further constrain the potential rates and Si sinks via authigenic clay formation in marine sedimentary environments.

Implications for reverse weathering rates and alkalinity sink

The reaction timescale, rate, and associated Si sink of reverse weathering have been consistently revised upward since the process was added to marine Si budgets in the early 2000s (80). The two milestone revisions updated the timescale of reverse weathering from thousands of years (21) to 20 to 36 months (5, 28) to 10 months (26, 29), while the upward revision of reverse weathering as a global Si sink increased from 0 to 1.5 to 4.5 to 4.9 Tmol/year (16, 17). The reverse weathering rates extrapolated were also updated to 1.3×10^{-6} (26) and 3.9×10^{-6} μmol/cm³ per s (17, 81) based on the Si uptake rates and the coupled consumption of Si and alkalinity during reverse weathering.

In this study, we demonstrated the rapid formation of Fe-rich smectite and mica within 40 days compared to the generally recognized 10 months (29). While it is important to acknowledge the challenges inherent in scaling rates derived under laboratory conditions to rates expected in the field, this is a necessary first step toward better constraining the rates and mechanisms of reverse weathering in marine sediments. We first apply a conventional simplified

zero-order reaction rate law (26) to the laboratory-derived rates and then scale to field rate approximation via bSi-to-sediment weight-to-weight ratio (see the “Reaction rate conversion to sediment condition” section in Materials and Methods), assuming typical bSi weight percent in sediments and average deltaic sediment density and porosity. This results in a Si(OH)₄ reaction rate of 35×10^{-6} μmol/cm³ per s (table S3).

The rates extrapolated from our experiments are about 10 times higher than the most recently updated reverse weathering rate of 3.9×10^{-6} μmol/cm³ per s (table S4) (10, 17, 81), in line with the ~1-month timescale compared to the previous observed ~10-month timescale. This elevated rate is particularly likely to be observed in regional areas such as deltaic environments, which the incubation conditions of this study are meant to closely mirror. We acknowledge that this rate may yield the upper boundary of the regional reverse weathering rate, as the reaction conditions in the field may limit rates relative to laboratory conditions. In particular, natural conditions that may lower reaction rates include lower reactant concentrations [Fe²⁺, Al(OH)₄⁻, dissolved Si(OH)₄, and other dissolved cations] and reaction pH. On the other hand, however, field rates can be accelerated via catalyzed authigenic mineral formation by pre-existing substrates (82, 83) or through microbial activity (84–86), although the latter is not involved under the abiotic conditions applied in this experiment. A recent study using sediment isotopic data combined with reactive transport modeling similarly reported locally high rates of reverse weathering across the Peruvian margin in response to local weather conditions (50). To our knowledge, this present study provides the first direct evidence to reveal the rapid occurrence of reverse weathering within 40 days. Note that we only examined the end product at day 40, and the time-course solution data, which are more sensitive than solid product measures, also suggest that authigenic clay precipitation occur at a timescales from within weeks to ~1 month. The finding indicates that reverse weathering reactions are more responsive than generally accepted and can affect marine cation and alkalinity sink on human timescale.

The formation of cation-rich (e.g., Li⁺, K⁺, Mg²⁺, and Fe²⁺) authigenic clay (e.g., excluding kaolinite) consumes alkalinity and release CO₂ (2, 3, 6, 8, 28) and thus plays a role in impacting the carbon cycling and Earth's climate (6, 8–10). CO₂ flux coupled with reverse weathering was estimated from a ratio of alkalinity flux to Si consumption (Alk/Si ratio) to constrain global carbon budgets both in Earth's history and the modern time via Earth system models (section S1) (8, 9). It was proposed that prolific reverse weathering before Precambrian performed as a long-term stabilizer of Earth's climate, although the proliferation of biogenic silica later resulted in declined silica-rich conditions that further dampened this role of reverse weathering (8). For the modern time, the upper boundary of CO₂ flux attributed by reverse weathering in recently reported modern global carbon cycle budget by Isson *et al.* (9) was built based on the updated Si budget (4.5 to 4.9 Tmol/year) by Rahman *et al.* (17, 81) (with corresponding extrapolated reverse weathering rates at 3.9×10^{-6} μmol/cm³ per s) (section S1 and table S5).

In light of the more rapid reverse weathering rates extrapolated in this study, re-evaluating the more robust roles and impacts of reverse weathering are needed to further unravel alkalinity and CO₂ dynamics. It would be important to quantitatively assess how elevated reverse weathering rates affect alkalinity sinks compared to previously reported. Would the elevated rates indicate a higher release of CO₂ in marine environments? Our results provide a mechanistic

basis to show that biogenic silica derived from diatom was conducive for rapid modern reverse weathering. In addition, how would different forms of silica including dissolved silica and biogenic silica derived from different Si-biomineralization species (e.g., radiolarians, sponges, diatoms, allochthonous grass phytoliths, etc.) behave in different environments across the continuum from continental to various marine environments in response to weathering inputs? More research is warranted to answer these questions.

Our findings also suggest that it is important to consider the robustness of reverse weathering when evaluating the effectiveness of anthropogenic interventions such as enhanced rock weathering for climate mitigation. Enhanced rock weathering has gained momentum as a strategy to remove CO₂ from the atmosphere and stabilize climate with initiated implementations in a variety of environments including croplands, coastal, and open ocean (87–89). There appears to be a strong capacity (i.e., the increased reverse weathering rate) to consume sedimentary Si and mineralized carbon (i.e., alkalinity) in marine sediments by this process; thus, geoengineering strategies [e.g., olivine dissolution (19, 20)] that propose CO₂ sequestration via silicate mineral weathering may have lower net drawdown in CO₂ if reverse weathering reactions can quickly consume the mineral-liberated Si and move CO₂ back into the system. Therefore, the net efficiency factor of these geoengineering climate solutions, along with the necessary adjustments (e.g., implementation pathway optimization), needs to be further modeled, constructed, and integrated into the measurement, reporting, and verification frameworks for carbon removal.

MATERIALS AND METHODS

Materials, experiments, and analyses

Solid-phase preparation and characterization

Two representative Fe- and Al-containing hydroxide minerals, ferrihydrite [Fe(OH)₃] and amorphous Al hydroxide [Al(OH)₃], respectively, were synthesized following previous procedures (90, 91). The marine diatom *Thalassiosira pseudonana* was used as a bSi source (Reed Mariculture Inc.) and stored at –20°C. Prior to use, biomass was thawed and repeatedly rinsed with deionized (DI) water (18 megohm-cm) to remove residual growth media. Rinsing started with the suspension of ~1 g of wet biomass in 50 ml of DI, followed by repeated shaking and centrifugation (2200g, 5 min) until the conductivity of the supernatant was constant and similar to that of DI water (<20 μS cm⁻¹). The rinsed material was freeze-dried and gently ground. Then, 0.2 g of the solid was placed in glass petri dishes for organic matter removal by low-temperature plasma ashing (Plasma-Therm RIE) for 7 hours at 350 W and 25°C and an O₂ flow rate of 60 standard cubic centimeters per minute, following our previous procedure (77). Compared to other common cleaning methods, our recent study showed that low-temperature plasma ashing preserves the degree of structural order of the SiO₂ framework, efficiently removes organic carbon, and is the least impactful on frustule dissolution compared to other cleaning methods such as high temperature and/or harsh chemical treatments (77).

The structures of Fe(OH)₃, Al(OH)₃, and bSi were characterized by XRD (PANalytical Empyrean, Cu Kα source). All three solid phases were confirmed to be x-ray amorphous (fig. S7). Organic carbon content of the plasma-cleaned bSi is 1.0 ± 0.09 weight % (wt %), measured by combustion using a CHNSO analyzer (Costech Instruments) after acid fuming over night (92). A portion of the cleaned

bSi was digested (0.2 M NaOH for 15 min at 100°C) (93), and the digestate was analyzed for Mg, K, Ca, Al, and Fe concentrations using inductively coupled plasma–mass spectrometry (ICP-MS; Agilent 7500a). The bSi contained 0.4 ± 0.1 wt % Fe, consistent with previously observed relative high concentrations of Fe incorporation into *T. pseudonana* frustules (94). Concentrations of Mg, K, Ca, and Al were below the detection limits [5 parts per billion (ppb)].

Batch experiments

Batch experiments were conducted under simulated sedimentary conditions with different combinations of Fe(OH)₃, Al(OH)₃, and bSi solids, each at 0.1 g/liter, suspended in anoxic artificial seawater (ASW) (95) (pH 7.5, buffered with 15 mM Hepes) with 150 μM Si(OH)₄. Anoxic DI water was prepared by ultraviolet (UV) sterilization and contributed bubbling with ultrahigh-purity nitrogen. The anoxic DI was then stored in the glove box (Coy; 95/5 N₂/H₂), allowing it to reach gas equilibrium with an oxygen concentration of 0 parts per million (ppm) and was subsequently used for the experiments and stock solution preparation. Experiments were conducted when oxygen level was at 0 ppm. Anoxic ASW was prepared in the glove box using the anoxic DI water. The experimental pH of 7.5 is similar to the condition of Amazon sediment pore waters (28). The addition of 150 μM dissolved Si(OH)₄ (as Na₂SiO₃) simulates the observed pore water Si(OH)₄ concentration for the upper 100 cm of Amazon Delta sediments (28) and Mississippi sediments (27, 35). Dissolved Fe(II) was added (as FeCl₂) to the reaction suspension at 0 μM, 100 μM [Amazon shelf deposit sediments (96)], or 1000 μM [representing its concentration in the upper 20 cm of Congo River fan sediments (47) and Amazon Delta porewaters (26)]. The use of amorphous Al(OH)₃ was based on the fact that Al(OH)₃ is usually a weathering product of Al-bearing lithogenic phases (97). The experiments were conducted at room temperature (25°C), similar to the temperature (28°C) reported for the Amazon Delta sediment (28).

Experiments were conducted in an anoxic glove box using custom-built polyvinyl chloride reactors (7.6 cm) with two chambers (bSi chamber and mineral chamber) separated by a dialysis membrane (12 to 14 kDa, 47 mm; Spectra/Por) (fig. S1). Each chamber contained 40-ml reaction suspension. The reactor assemblies were acid washed and UV-sterilized before use. Two sets of experimental groups were set up, with or without bSi. Experimental conditions and sample labels are summarized in Table 1 for group I with bSi and table S1 for groups II and III without bSi. For group I, the bSi substrate was contained in one chamber and the Al/Fe hydroxides in the other chamber, such that any transformation involving Al/Fe hydroxides can be attributed to a dissolution–reprecipitation reaction. This also allowed the sampling and structural characterization of transformation products of bSi without the interference from the Al/Fe hydroxides. For groups II and III, a set of control experiment was conducted with 150 μM dissolved Si(OH)₄ (dSi), instead of bSi, with or without Al/Fe hydroxides. An additional control experiment was conducted with no bSi and only dissolved phases of 150 μM Si(OH)₄ (as Na₂SiO₃), 100 μM Fe(II) (as FeCl₂), and 30 μM Al³⁺ (as AlCl₃). All experiments were conducted in duplicates. Experimental conditions and sample labels are summarized in Table 1 for group I (with bSi) and table S1 for groups II and III (without bSi).

Sample-loaded reactors were constantly agitated on a shaker table (120 rpm), assuming that the concentration of ions at each side of the chamber were homogenized through constant shaking. Mixing times when chambers are rolled slowly (e.g., 2 rpm) is on the

order of 1 day (fig. S6); therefore, the shaking likely facilitated well-mixed conditions. The mineral chamber (loaded with Al/Fe hydroxides) had a hole at the end, which was sealed with silicone stoppers and epoxy. Aliquots of the suspensions were collected periodically using a 1-mm needle through the silicone stoppers, and the liquids were syringe filtered (0.1 μm , PTFE) and analyzed for solution composition. At the end of reactions, final solid phases were harvested from both chambers, repeatedly rinsed with anoxic DI water under vacuum filtration, dried in the glove box, and characterized for morphological and structural features.

Aqueous phase analyses

At each sampling point, dissolved total Fe (Fe_T) and Fe(II) were quantified using the ferrozine spectrophotometric method with or without hydroxylamine, respectively (98). Dissolved $\text{Si}(\text{OH})_4$ was quantified with the molybdenum blue spectrophotometric method (99) using a UV-visible spectrometry (Cary 60, Agilent). Concentrations of dissolved Al were measured by ICP-MS (Agilent 7500a) with a detection limit of 5 ppb.

Solid-phase analyses

For experimental groups containing bSi, reacted solids from both chambers were dried on filter membranes inside the anoxic glove box (95/5 N_2/H_2 , Coy). Solid phases from the bSi chamber were characterized for bSi morphology using SEM (Hitachi SU-8230) and EDX. For groups showing signs of authigenic phase formation under SEM, the solids from both sides of the chamber were further characterized by synchrotron XRD and HRTEM. For synchrotron XRD analysis, solids were sealed into glass capillaries inside the glove box, and the data were collected at Beamline 17-BM-B ($\lambda = 0.39433 \text{ \AA}$) at Advanced Photon Source (Argonne National Laboratory, Lemont, IL). Based on XRD analysis, the solids at the bSi chamber of the 1000Fe(II) + bSi + Al group showed signs of authigenic clay phase formation and were further analyzed and compared with a control group 1000Fe(II) + bSi using HRTEM (JEOL JEM-2100 LaB6 TEM, 200-keV accelerating voltage), SAED (Gatan Orius SC200D camera), and EDX (Bruker AXS Microanalysis Quantax 200 with 4030 SDD detector).

Converting Si reaction rate from laboratory experiments to marine sedimentary conditions

Reaction rate obtained from laboratory experiments

To compare laboratory results with field data, we define the reaction rate in laboratory experiment as the change in reacted concentration over time, which is similar to field studies that estimate and ascribe observed Si fluxes at seasonal timescales (26). As the measured $[\text{Si}(\text{OH})_4]$ is affected by both dissolution and reprecipitation, which cannot fully represent the reacted $\text{Si}(\text{OH})_4$, the $\text{Si}(\text{OH})_4$ reaction rate we calculated here was based on reacted Fe^{2+} concentration within our experimental time frame and Fe/Si ratios of authigenic clay products. The cation/Si ratio is commonly used in field studies as a reliable metric to estimate the rate of Si uptake during the formation of authigenic clays, resulting from the alteration of bSi (26). Our experiment monitored the reaction for over a month, and the Fe-smectite and mica authigenic clay products were observed to have formed over 1 month. We then define the reaction time as 1 month and first calculated monthly reaction rate. The monthly reaction rate of dissolved $\text{Si}(\text{OH})_4$ during the transformation of bSi to authigenic clay was estimated on the basis of the amount of reacted Fe^{2+} within 1 month [$\sim 500 \mu\text{M}$ for treatment 1000Fe(II) + bSi + Al] and the Fe/Si ratio in the reaction products (detailed in Eqs. 2 and 3 below). The

obtained monthly rate was then converted to a yearly rate by multiplying by 12 (Eq. 4). For Fe-smectite and mica, the literature reported stoichiometric Fe/Si ratio of pure Fe-smectite phase is ~ 0.5 and ~ 1 for pure Fe-rich muscovite. For authigenic products observed from previous field extraction and SEM studies, this ratio typically varies with an average value of ~ 0.13 (26). This value is a lump sum of different Fe-bearing authigenic products such as intermediate or immature authigenic products. The Fe/Si ratio in the authigenic products in this study observed by SEM varied at 0.2 to 0.9, with an average of 0.42. Thus, we used a value of 0.42 for Fe/Si ratio. The calculated $\text{Si}(\text{OH})_4$ rates with a unit of μM per month directly derived from the experimental data are displayed in table S3.

Reaction rate conversion to sediment condition

The translation of $\text{Si}(\text{OH})_4$ reaction rate from laboratory conditions to field sedimentary conditions is based on the laboratory experimental conditions, a field observed average porosity of ~ 0.7 , and sediment density of 2.6 g/cm^3 (26), with the assumptions that our experimental conditions are comparable to deltaic environments with sufficient Fe and Al hydroxide supplies (26, 35) [e.g., the highest Fe^{2+} treatment at $\sim 1000 \mu\text{M}$ (47) and dissolved Al at micromolar level (50)]. To be comparable to estimated field sediment Si flux rate, which is measured by reacted $\text{Si}(\text{OH})_4$ over dry sediment solid mass with units of $\mu\text{mol/g}$ per year or $\mu\text{mol/cm}^3$ per year (interchangeable by average sediment density) (26, 81), we then ascribe the reacted solutes to comparable amounts of sediment solid volume in field sediment condition. With weight percentage of typical bSi concentration in marine sediments at 1 to 2 wt % (26, 63), this method assumes a bSi concentration of 1 wt %. Then, the 0.1 g of bSi used in this study is ascribed to 10 g of sediments. Applying an average sediment bulk density of $0.78 \text{ g solid/cm}^3$ (porosity of 0.7 and particle solid density of 2.6 g/cm^3) typical for delta environments (26), 10 g of dry sediment has a total wet volume of 12.8 cm^3 . Therefore, the reacted $\text{Si}(\text{OH})_4$ corresponds to 12.8 cm^3 of sediment (Eq. 5), as observed in the extraction of dry sediment solids. The converted $\text{Si}(\text{OH})_4$ rate was summarized in table S3.

Monthly Fe^{2+} reaction rate at laboratory condition ($\mu\text{M}/\text{month}$) can be calculated as

$$\frac{d(\text{Fe}^{2+})}{dt} = \frac{\text{Reacted Fe}^{2+}}{\text{time}} = \frac{500 \mu\text{M}}{1 \text{ month}} \quad (2)$$

Monthly $\text{Si}(\text{OH})_4$ reaction rate at laboratory condition ($\mu\text{M}/\text{month}$) can be calculated as

$$\frac{1}{f} * \frac{d(\text{Fe}^{2+})}{dt} = \frac{1}{s} * \frac{d[\text{Si}(\text{OH})_4]}{dt} \quad (3)$$

where f/s denotes Fe/Si ratio in authigenic phase.

Yearly $\text{Si}(\text{OH})_4$ reaction rate at laboratory condition ($\mu\text{M}/\text{year}$) can be calculated as

$$= \text{Si}(\text{OH})_4 \text{ reaction rate at laboratory condition per month} * 12 \text{ months/1 year} \quad (4)$$

Yearly $\text{Si}(\text{OH})_4$ reaction rate at field sedimentary condition ($\mu\text{mol/cm}^3$ per year) can be calculated as

$$\frac{\text{Yearly Si}(\text{OH})_4 \text{ reaction rate at laboratory condition in } \mu\text{M}/\text{year} * 1 \text{ liter}}{12.8 \text{ cm}^3} = \frac{\text{Si}(\text{OH})_4 \text{ reaction rate at lab condition in } \mu\text{mol}/\text{year}}{12.8 \text{ cm}^3} \quad (5)$$

Estimation of reverse weathering rate

The $\text{Si}(\text{OH})_4$ consumption is coupled with alkalinity consumption to form authigenic clay; therefore, the Si consumption rate is considered equivalent to the rate of authigenic clay formation (26). Assuming the reaction rate (R) of reverse weathering is zero order with respect to dissolved $\text{Si}(\text{OH})_4$ (26), i.e., $R = k_{RW} * [\text{Si}(\text{OH})_4]^0$, then the reaction rate R derived as (Eq. 6)

$$-\frac{d[\text{Si}(\text{OH})_4]}{dt} = R \quad (6)$$

The silicon uptake rate or reverse weathering rate can be an indication of an effective reverse weathering coefficient (k_{RW}) around this order of magnitude for comparable reaction conditions (10). Thus, the rate can be calculated in $\mu\text{mol}/\text{cm}^3/\text{s}$ and compared with literature reverse weathering reaction rates and rate coefficients (table S4) to indicate the magnitude of reverse weathering rates.

Supplementary Materials**The PDF file includes:**

Section S1
Figs. S1 to S7
Tables S1 to S5
Legend for data S1
References

Other Supplementary Material for this manuscript includes the following:

Data S1

REFERENCES AND NOTES

- R. M. Garrels, Silica: Role in the buffering of natural waters. *Science* **148**, 69–69 (1965).
- F. T. Mackenzie, R. M. Garrels, Chemical mass balance between rivers and oceans. *Am. J. Sci.* **264**, 507–525 (1966).
- F. T. Mackenzie, R. M. Garrels, Silica-bicarbonate balance in the ocean and early diagenesis. *J. Sediment. Res.* **36**, 1075–1084 (1966).
- F. T. Mackenzie, R. M. Garrels, O. P. Bricker, F. Bickley, Silica in sea water: Control by silica minerals. *Science* **155**, 1404–1405 (1967).
- P. Michalopoulos, R. C. Aller, R. J. Reeder, Conversion of diatoms to clays during early diagenesis in tropical, continental shelf muds. *Geology* **28**, 1095–1098 (2000).
- A. G. Dunlea, R. W. Murray, D. P. Santiago Ramos, J. A. Higgins, Cenozoic global cooling and increased seawater Mg/Ca via reduced reverse weathering. *Nat. Commun.* **8**, 844 (2017).
- T. Isson, S. Rauzi, Oxygen isotope ensemble reveals Earth's seawater, temperature, and carbon cycle history. *Science* **383**, 666–670 (2024).
- T. T. Isson, N. J. Planavsky, Reverse weathering as a long-term stabilizer of marine pH and planetary climate. *Nature* **560**, 471–475 (2018).
- T. T. Isson, N. J. Planavsky, L. A. Coogan, E. M. Stewart, J. J. Ague, E. W. Bolton, S. Zhang, N. R. McKenzie, L. R. Kump, Evolution of the global carbon cycle and climate regulation on Earth. *Global Biogeochem. Cycles* **34**, e2018GB006061 (2020).
- J. Krissansen-Totton, D. C. Catling, A coupled carbon-silicon cycle model over Earth history: Reverse weathering as a possible explanation of a warm mid-Proterozoic climate. *Earth Planet. Sci. Lett.* **537**, 116181 (2020).
- D. P. Santiago Ramos, L. E. Morgan, N. S. Lloyd, J. A. Higgins, Reverse weathering in marine sediments and the geochemical cycle of potassium in seawater: Insights from the K isotopic composition (41K/39K) of deep-sea pore-fluids. *Geochim. Cosmochim. Acta* **236**, 99–120 (2018).
- X. Sun, J. Higgins, A. V. Turchyn, Diffusive cation fluxes in deep-sea sediments and insight into the global geochemical cycles of calcium, magnesium, sodium and potassium. *Mar. Geol.* **373**, 64–77 (2016).
- A. Baldermann, S. Banerjee, G. Czuppon, M. Dietzel, J. Farkaš, S. Lühr, U. Moser, E. Scheibhofer, N. M. Wright, T. Zack, Impact of green clay authigenesis on element sequestration in marine settings. *Nat. Commun.* **13**, 1527 (2022).
- M. Guo, J. Korenaga, Rapid rise of early ocean pH under elevated weathering rates. *Nat. Geosci.* **18**, 260–266 (2025).
- P. J. Tréguer, J. N. Sutton, M. Brzezinski, M. A. Charette, T. Devries, S. Dutkiewicz, C. Ehler, J. Hawkings, A. Leynaert, S. M. Liu, N. Llopis Monferrer, M. López-Acosta, M. Maldonado, S. Rahman, L. Ran, O. Rouxel, Reviews and syntheses: The biogeochemical cycle of silicon in the modern ocean. *Biogeochemistry* **18**, 1269–1289 (2021).
- P. J. Tréguer, C. L. De La Rocha, in *Annual Review of Marine Science*, C. A. Carlson, S. J. Giovannoni, Eds. (Annual Reviews, 2013), vol. 5, pp. 477–501.
- S. Rahman, R. C. Aller, J. K. Cochran, The missing silica sink: Revisiting the marine sedimentary Si cycle using cosmogenic ^{32}Si . *Global Biogeochem. Cycles* **31**, 1559–1578 (2017).
- O. Ragueneau, D. J. Conley, D. J. DeMaster, H. H. Durr, N. Dittert, in *Carbon and Nutrient Fluxes in Continental Margins: A Global Synthesis*, K. K. Liu, L. Atkinson, R. Quinones, L. TalaeMcManus, Eds. (Springer, 2010), pp. 515–527.
- S. Foteinis, J. S. Campbell, P. Renforth, Life cycle assessment of coastal enhanced weathering for carbon dioxide removal from air. *Environ. Sci. Technol.* **57**, 6169–6178 (2023).
- Y. Kanzaki, N. J. Planavsky, C. T. Reinhard, New estimates of the storage permanence and ocean co-benefits of enhanced rock weathering. *PNAS Nexus* **2**, pgad059 (2023).
- G. S. Odin, F. Fröhlich, Chapter C3 Glaucony from the Kerguelen Plateau (southern Indian Ocean). *Dev. Sedimentol.* **45**, 277–294 (1988).
- J. E. Mackin, Control of dissolved Al distributions in marine-sediments by clay reconstitution reactions - experimental-evidence leading to a unified theory. *Geochim. Cosmochim. Acta* **50**, 207–214 (1986).
- J. E. Mackin, R. C. Aller, Dissolved Al in sediments and waters of the east China Sea—Implications for authigenic mineral formation. *Geochim. Cosmochim. Acta* **48**, 281–297 (1984).
- J. E. Mackin, R. C. Aller, THE effects of clay mineral reactions on dissolved Al distributions in sediments and waters of the amazon continental-shelf. *Cont. Shelf Res.* **6**, 245–262 (1986).
- J. R. Hein, H.-W. Yeh, E. Alexander, Origin of iron-rich montmorillonite from the manganese nodule belt of the North Equatorial Pacific. *Clays Clay Miner.* **27**, 185–194 (1979).
- P. Michalopoulos, R. C. Aller, Early diagenesis of biogenic silica in the Amazon delta: Alteration, authigenic clay formation, and storage. *Geochim. Cosmochim. Acta* **68**, 1061–1085 (2004).
- R. A. Pickering, L. Cassarino, K. R. Hendry, X. L. Wang, K. Maiti, J. W. Krause, Using stable isotopes to disentangle marine sedimentary signals in reactive silicon pools. *Geophys. Res. Lett.* **47**, e2020GL087877 (2020).
- P. Michalopoulos, R. C. Aller, Rapid clay mineral formation in Amazon delta sediments: Reverse weathering and oceanic elemental cycles. *Science*, 614–617 (1995).
- S. Loucaides, P. Michalopoulos, M. Presti, E. Koning, T. Behrends, P. Van Cappellen, Seawater-mediated interactions between diatomaceous silica and terrigenous sediments: Results from long-term incubation experiments. *Chem. Geol.* **270**, 68–79 (2010).
- R. S. Arvidson, F. T. Mackenzie, M. Guidry, MAGIC: A Phanerozoic model for the geochemical cycling of major rock-forming components. *Am. J. Sci.* **306**, 135–190 (2006).
- A. Baldermann, L. N. Warr, I. Letofsky-Papst, V. Mavromatis, Substantial iron sequestration during green-clay authigenesis in modern deep-sea sediments. *Nat. Geosci.* **8**, 885–889 (2015).
- K. L. Russell, Geochemistry and halmyrolysis of clay minerals, Rio-Ameca, Mexico. *Geochim. Cosmochim. Acta* **34**, 893–907 (1970).
- J. I. Drever, Early diagenesis of clay minerals, Rio-Ameca Basin, Mexico. *J. Sediment. Petrol.* **41**, 982–994 (1971).
- F. T. Mackenzie, L. R. Kump, Reverse weathering, clay mineral formation, and oceanic element cycles. *Science* **270**, 586 (1995).
- M. Presti, P. Michalopoulos, Estimating the contribution of the authigenic mineral component to the long-term reactive silica accumulation on the western shelf of the Mississippi River Delta. *Cont. Shelf Res.* **28**, 823–838 (2008).
- R. C. Aller, in *Treatise on Geochemistry*, H. H. D., T. K.K., Eds. (Elsevier, ed. 2, 2014), vol. 8, pp. 293–334.
- S. M. Chemtob, R. D. Nickerson, R. V. Morris, D. G. Agresti, J. G. Catalano, Synthesis and structural characterization of ferrous trioctahedral smectites: Implications for clay mineral genesis and detectability on Mars. *J. Geophys. Res. Planets* **120**, 1119–1140 (2015).
- D. M. Moore, *X-Ray Diffraction and the Identification and Analysis of Clay Minerals*, D. M. Moore, R. C. Reynolds Jr., Eds. (Oxford Univ. Press, 1989).
- W. D. Keller, R. C. Reynolds, A. Inoue, Morphology of clay minerals in the smectite-to-illite conversion series by scanning electron microscopy. *Clays Clay Miner.* **34**, 187–197 (1986).
- G. J. Redhammer, A. Beran, J. Schneider, G. Amthauer, W. Lottermoser, Spectroscopic and structural properties of synthetic micas on the annite-siderophyllite binary: Synthesis, crystal structure refinement, Mössbauer, and infrared spectroscopy. *Am. Mineral.* **85**, 449–465 (2000).
- M. J. Holdaway, Chemical formulae and activity models for biotite, muscovite, and chlorite applicable to pelitic metamorphic rocks. *Am. Mineral.* **65**, 711–719 (1980).

42. M. Gharrabi, B. Velde, J. P. Sagon, The transformation of illite to muscovite in pelitic rocks: Constraints from X-Ray diffraction. *Clays Clay Miner.* **46**, 79–88 (1998).
43. J. P. Gustafsson, Visual MINTEQ (Stockholm, 2016).
44. D. Rickert, M. Schlüter, K. Wallmann, Dissolution kinetics of biogenic silica from the water column to the sediments. *Geochim. Cosmochim. Acta* **66**, 439–455 (2002).
45. P. Van Cappellen, L. Q. Qiu, Biogenic silica dissolution in sediments of the Southern Ocean. II. Kinetics. *Deep Sea Res. II Top. Stud. Oceanogr.* **44**, 1129–1149 (1997).
46. D. L. Parkhurst, "User's guide to PHREEQC, a computer program for speciation, reaction-path, advective-transport, and inverse geochemical calculations," *Water-Resources Investigations Report* (U.S. Geological Survey, 1995).
47. J. S. Beckler, N. Kiriazis, C. Rabouille, F. J. Stewart, M. Taillefert, Importance of microbial iron reduction in deep sediments of river-dominated continental-margins. *Mar. Chem.* **178**, 22–34 (2016).
48. R. W. Gensemer, R. C. Playle, The bioavailability and toxicity of aluminum in aquatic environments. *Crit. Rev. Environ. Sci. Technol.* **29**, 315–450 (1999).
49. K. G. Wallmann, S. Geilert, F. Scholz, Chemical alteration of riverine particles in seawater and marine sediments: Effects on seawater composition and atmospheric CO₂. *Am. J. Sci.* **323**, 7 (2023).
50. S. Geilert, D. A. Frick, D. Garbe-Schönberg, F. Scholz, S. Sommer, P. Grasse, C. Vogt, A. W. Dale, Coastal El Niño triggers rapid marine silicate alteration on the seafloor. *Nat. Commun.* **14**, 1676 (2023).
51. K. M. Mkadam, T. Yonaha, V. S. Ali, A. Tokuyama, Dissolved aluminum and silica release on the interaction of Okinawan subtropical red soil and seawater at different salinities: Experimental and field observations. *Geochem. J.* **40**, 333–343 (2006).
52. P. Van Cappellen, S. Dixit, J. van Beusekom, Biogenic silica dissolution in the oceans: Reconciling experimental and field-based dissolution rates. *Global Biogeochem. Cycles* **16**, 23-1-23-10 (2002).
53. O. Ragueneau, S. Schultes, K. Bidle, P. Clauquin, B. La Moriceau, Si and C interactions in the world ocean: Importance of ecological processes and implications for the role of diatoms in the biological pump. *Global Biogeochem. Cycles* **20**, GB4502 (2006).
54. M. Maldonado, M. López-Acosta, C. Sijth, M. García-Puig, C. Galobart, G. Ercilla, A. Leynaert, Sponge skeletons as an important sink of silicon in the global oceans. *Nat. Geosci.* **12**, 815–822 (2019).
55. D. E. Canfield, K. Erik, T. Bo, in *Advances in Marine Biology*, D. E. Canfield, E. Kristensen, B. Thamdrup, Eds. (Academic Press, 2005), vol. 48, pp. 441–463.
56. N. Llopis Monferrer, D. Boltovskoy, P. Tréguer, M. M. Sandin, F. Not, A. Leynaert, Estimating biogenic silica production of rhizaria in the global ocean. *Global Biogeochem. Cycles* **34**, e2019GB006286 (2020).
57. P. Van Cappellen, L. Q. Qiu, Biogenic silica dissolution in sediments of the Southern Ocean. I. Solubility. *Deep Sea Res. II Top. Stud. Oceanogr.* **44**, 1109–1128 (1997).
58. S. Dixit, P. Van Cappellen, Surface chemistry and reactivity of biogenic silica. *Geochim. Cosmochim. Acta* **66**, 2559–2568 (2002).
59. J. C. Lewin, The dissolution of silica from diatom walls. *Geochim. Cosmochim. Acta* **21**, 182–198 (1961).
60. R. K. Iler, *The Chemistry of Silica*. (Wiley- Interscience, 1979).
61. A. J. Vanbennekum, J. H. F. Jansen, S. J. Vandergaast, J. M. Vaniperen, J. Pieters, Aluminum-rich opal—An intermediate in the preservation of biogenic silica in the Zaire (Congo) deep-sea fan. *Deep Sea Res. I Oceanogr. Res. Pap.* **36**, 173–190 (1989).
62. M. Kosmulski, *Surface charging and points of zero charge*. Surfactant science series (CRC Press, 2009), p. 27.
63. C. Ehlert, K. Doering, K. Wallmann, F. Scholz, S. Sommer, P. Grasse, S. Geilert, M. Frank, Stable silicon isotope signatures of marine pore waters—Biogenic opal dissolution versus authigenic clay mineral formation. *Geochim. Cosmochim. Acta* **191**, 102–117 (2016).
64. P. Frings, Revisiting the dissolution of biogenic Si in marine sediments: A key term in the ocean Si budget. *Acta Geochimica* **36**, 429–432 (2017).
65. N. J. Tosca, S. Guggenheim, P. K. Pufahl, An authigenic origin for Precambrian greenalite: Implications for iron formation and the chemistry of ancient seawater. *GSA Bull.* **128**, 511–530 (2016).
66. K. Laufer, J. M. Byrne, C. Glombitza, C. Schmidt, B. B. Jørgensen, A. Kappler, Anaerobic microbial Fe(II) oxidation and Fe(III) reduction in coastal marine sediments controlled by organic carbon content. *Environ. Microbiol.* **18**, 3159–3174 (2016).
67. X. Zhang, J. Gaillardet, L. Barrier, J. Bouchez, Li and Si isotopes reveal authigenic clay formation in a palaeo-delta. *Earth Planet. Sci. Lett.* **578**, 117339 (2022).
68. D. Badaut, F. Risacher, Authigenic smectite on diatom frustules in Bolivian saline lakes. *Geochim. Cosmochim. Acta* **47**, 363–375 (1983).
69. N. J. Tosca, F. A. Macdonald, J. V. Strauss, D. T. Johnston, A. H. Knoll, Sedimentary talc in Neoproterozoic carbonate successions. *Earth Planet. Sci. Lett.* **306**, 11–22 (2011).
70. M. Pozo, J. P. Calvo, An overview of authigenic magnesium clays. *Minerals* **8**, 520 (2018).
71. J. Tosca Nicholas, V. P. Wright, Diagenetic pathways linked to labile Mg-clays in lacustrine carbonate reservoirs: A model for the origin of secondary porosity in the Cretaceous pre-salt Barra Velha Formation, offshore Brazil. *Geol. Soc. Lond. Spec. Publ.* **435**, 33–46 (2018).
72. J. Kim, H. Dong, K. Yang, H. Park, W. C. Elliott, A. Spivack, T. Koo, G. Kim, Y. Morono, S. Henkel, F. Inagaki, Q. Zeng, T. Hoshino, V. B. Heuer, Naturally occurring, microbially induced smectite-to-illite reaction. *Geology* **47**, 535–539 (2019).
73. M. Robert, The experimental transformation of mica toward Smectite; relative importance of total charge and tetrahedral substitution. *Clays Clay Miner.* **21**, 167–174 (1973).
74. B. Velde, in *Treatise on Geochemistry*, H. D. Holland, K. K. Turekian, Eds. (Elsevier, ed. 2, 2014), pp. 351–364.
75. J. E. Mackin, R. C. Aller, Diagenesis of dissolved aluminum in organic-rich estuarine sediments. *Geochim. Cosmochim. Acta* **48**, 299–313 (1984).
76. K. D. Bidle, F. Azam, Bacterial control of silicon regeneration from diatom detritus: Significance of bacterial ectohydrolases and species identity. *Limnol. Oceanogr.* **46**, 1606–1623 (2001).
77. E. M. Saad, R. A. Pickering, K. Shoji, M. I. Hossain, T. G. Glover, J. W. Krause, Y. Tang, Effect of cleaning methods on the dissolution of diatom frustules. *Mar. Chem.* **224**, 103826 (2020).
78. D. J. DeMaster, in *Treatise on Geochemistry*, H. D. Holland, K. K. Turekian, Eds. (Pergamon, 2003), pp. 87–98.
79. F. Fraysse, O. S. Pokrovsky, J. Schott, J.-D. Meunier, Surface chemistry and reactivity of plant phytoliths in aqueous solutions. *Chem. Geol.* **258**, 197–206 (2009).
80. G. G. Laruelle, V. Roubex, A. Sfratore, B. Brodherr, D. Ciuffa, D. J. Conley, H. H. Durr, J. Garnier, C. Lancelot, Q. L. T. Phuong, J. D. Meunier, M. Meybeck, P. Michalopoulos, B. Moriceau, S. N. Longphuir, S. Loucaides, L. Papush, M. Presti, O. Ragueneau, P. Regnier, L. Saccone, C. P. Slomp, C. Spiteri, P. Van Cappellen, Anthropogenic perturbations of the silicon cycle at the global scale: Key role of the land-ocean transition. *Global Biogeochem. Cycles* **23**, GB4031 (2009).
81. S. Rahman, R. C. Aller, J. K. Cochran, Cosmogenic ³²Si as a tracer of biogenic silica burial and diagenesis: Major deltaic sinks in the silica cycle. *Geophys. Res. Lett.* **43**, 7124–7132 (2016).
82. P. A. Maurice, *Environmental surfaces and interfaces from the nanoscale to the global scale*. (Wiley, 2009).
83. W. Stumm, J. J. Morgan, *Aquatic chemistry: Chemical equilibria and rates in natural waters*. (Wiley, ed. 3rd, 1996).
84. J. Aubineau, A. El Albani, A. Bekker, A. Somogyi, O. M. Bankole, R. Macchiarelli, A. Meunier, A. Riboulleau, J.-Y. Reynaud, K. O. Konhauser, Microbially induced potassium enrichment in Paleoproterozoic shales and implications for reverse weathering on early Earth. *Nat. Commun.* **10**, 2670 (2019).
85. J. Cuadros, Clay minerals interaction with microorganisms: A review. *Clay Miner.* **52**, 235–261 (2017).
86. M. Ueshima, K. Tazaki, Possible role of microbial polysaccharides in nontronite formation. *Clays Clay Miner.* **49**, 292–299 (2001).
87. D. J. Beerling, E. P. Kantzas, M. R. Lomas, P. Wade, R. M. Eufrazio, P. Renforth, B. Sarkar, M. G. Andrews, R. H. James, C. R. Pearce, J.-F. Mercure, H. Pollitt, P. B. Holden, N. R. Edwards, M. Khanna, L. Koh, S. Quegan, N. F. Pidgeon, I. A. Janssens, J. Hansen, S. A. Banwart, Potential for large-scale CO₂ removal via enhanced rock weathering with croplands. *Nature* **583**, 242–248 (2020).
88. F. J. Holden, K. Davies, M. I. Bird, R. Hume, H. Green, D. J. Beerling, P. N. Nelson, In-field carbon dioxide removal via weathering of crushed basalt applied to acidic tropical agricultural soil. *Sci. Total Environ.* **955**, 176568 (2024).
89. L. L. Taylor, J. Quirk, R. M. S. Thorley, P. A. Kharcha, J. Hansen, A. Ridgwell, M. R. Lomas, S. A. Banwart, D. J. Beerling, Enhanced weathering strategies for stabilizing climate and averting ocean acidification. *Nat. Clim. Chang.* **6**, 402–406 (2016).
90. Y. Z. Tang, F. M. Michel, L. H. Zhang, R. Harrington, J. B. Parise, R. J. Reeder, Structural properties of the Cr(III)-Fe(III) (Oxy)hydroxide compositional series: Insights for a nanomaterial "Solid Solution". *Chem. Mat.* **22**, 3589–3598 (2010).
91. T. Isobe, T. Watanabe, J. B. D. de la Caillerie, A. P. Legrand, D. Massiot, Solid-state H-1 and Al-27 NMR studies of amorphous aluminum hydroxides. *J. Colloid Interface Sci.* **261**, 320–324 (2003).
92. J. I. Hedges, J. H. Stern, Carbon and nitrogen determinations of carbonate-containing solids. *Limnol. Oceanogr.* **29**, 657–663 (1984).
93. G. L. Krause, C. L. Schelske, C. O. Davis, Comparison of three wet-alkaline methods of digestion of biogenic silica in water. *Freshw. Biol.* **13**, 73–81 (1983).
94. M. J. Ellwood, K. A. Hunter, The incorporation of zinc and iron into the frustule of the marine diatom *Thalassiosira pseudonana*. *Limnol. Oceanogr.* **45**, 1517–1524 (2000).
95. D. R. Kester, I. W. Duedall, D. N. Connors, R. M. Pytkowic, Preparation of artificial seawater. *Limnol. Oceanogr.* **12**, 176–179 (1967).
96. R. C. Aller, N. E. Blair, Q. Xia, P. D. Rude, Remineralization rates, recycling, and storage of carbon in Amazon shelf sediments. *Cont. Shelf Res.* **16**, 753–786 (1996).
97. M. Kawano, K. Tomita, Amorphous aluminum hydroxide formed at the earliest weathering stages of K-Feldspar. *Clays Clay Miner.* **44**, 672–676 (1996).

98. L. L. Stookey, Ferrozine—A new spectrophotometric reagent for iron. *Anal. Chem.* **42**, 779–781 (1970).
99. J. D. Strickland, T. R. Parsons, *A practical handbook of seawater analysis* (Fisheries Research Board of Canada, 1972).
100. K. Wallmann, G. Aloisi, M. Haeckel, P. Tishchenko, G. Pavlova, J. Greinert, S. Kutterolf, A. Eisenhauer, Silicate weathering in anoxic marine sediments. *Geochim. Cosmochim. Acta* **72**, 2895–2918 (2008).
101. J. A. Becker, M. J. Bickle, A. Galy, T. J. B. Holland, Himalayan metamorphic CO₂ fluxes: Quantitative constraints from hydrothermal springs. *Earth Planet. Sci. Lett.* **265**, 616–629 (2008).
102. E. M. Stewart, J. J. Ague, Infiltration-driven metamorphism, New England, USA: Regional CO₂ fluxes and implications for Devonian climate and extinctions. *Earth Planet. Sci. Lett.* **489**, 123–134 (2018).
103. P. B. Kelemen, C. E. Manning, Reevaluating carbon fluxes in subduction zones, what goes down, mostly comes up. *Proc. Natl. Acad. Sci. U.S.A.* **112**, E3997–E4006 (2015).
104. R. Dasgupta, M. M. Hirschmann, The deep carbon cycle and melting in Earth's interior. *Earth Planet. Sci. Lett.* **298**, 1–13 (2010).
105. D. R. Hilton, T. P. Fischer, B. Marty, Noble gases and volatile recycling at subduction zones. *Rev. Mineral. Geochem.* **47**, 319–370 (2002).
106. B. Marty, I. N. Tolstikhin, CO₂ fluxes from mid-ocean ridges, arcs and plumes. *Chem. Geol.* **145**, 233–248 (1998).
107. S. Matthews, O. Shorttle, J. F. Rudge, J. Maclennan, Constraining mantle carbon: CO₂-trace element systematics in basalts and the roles of magma mixing and degassing. *Earth Planet. Sci. Lett.* **480**, 1–14 (2017).
108. A. E. Saal, E. H. Hauri, C. H. Langmuir, M. R. Perfit, Vapour undersaturation in primitive mid-ocean-ridge basalt and the volatile content of Earth's upper mantle. *Nature* **419**, 451–455 (2002).
109. J. Gaillardet, B. Dupré, P. Louvat, C. J. Allègre, Global silicate weathering and CO₂ consumption rates deduced from the chemistry of large rivers. *Chem. Geol.* **159**, 3–30 (1999).
110. G. Li, H. Elderfield, Evolution of carbon cycle over the past 100 million years. *Geochim. Cosmochim. Acta* **103**, 11–25 (2013).
111. L. A. Coogan, K. M. Gillis, Low-temperature alteration of the seafloor: Impacts on ocean chemistry. *Annu. Rev. Earth Planet. Sci.* **46**, 21–45 (2018).
112. K. Wallmann, E. Pinero, E. Burwicz, M. Haeckel, C. Hensen, A. Dale, L. Ruepke, The global inventory of methane hydrate in marine sediments: A theoretical approach. *Energies* **5**, 2449–2498 (2012).
113. X. Sun, A. V. Turchyn, Significant contribution of authigenic carbonate to marine carbon burial. *Nat. Geosci.* **7**, 201–204 (2014).

Acknowledgments: We thank the reviewers whose comments helped to improve this manuscript. **Funding:** This work is funded by the National Science Foundation grants OCE-1559087 (to Y.T.) and OCE-1558957 (to J.W.K.). **Author contributions:** Conceptualization: S.Z., E.M.S., R.A.P., Y.T., J.W.K., E.I., M.T., and C.T.R. Methodology: E.M.S., S.Z., PL, R.A.P., Y.T., H.Z., H.D., and E.I. Investigation: E.M.S., S.Z., R.A.P., Y.T., H.Z., L.Z., and H.D. Formal analysis: S.Z., E.M.S., and P.L. Validation: S.Z., E.M.S., R.A.P., and Y.T. Visualization: S.Z., E.M.S., Y.T., and H.Z. Resources: Y.T., J.W.K., S.Z., E.M.S., H.D., E.I., and M.T. Data curation: S.Z. and E.M.S. Software: E.M.S. Funding acquisition: Y.T. and J.W.K. Supervision: Y.T. and J.W.K. Project administration: Y.T. Writing—original draft: S.Z., E.M.S., and H.D. Writing—review and editing: S.Z., E.M.S., R.A.P., Y.T., J.W.K., E.I., H.D., M.T., and C.T.R. **Competing interests:** The authors declare that they have no competing interests. **Data and materials availability:** All data need to evaluate the conclusions in the paper are present in the paper and/or the Supplementary Materials, which includes a PDF file for Supplementary text and figures and an Excel file for compiled solution phase data and EDX data.

Submitted 23 September 2024

Accepted 2 October 2025

Published 29 October 2025

10.1126/sciadv.adt3374